Buried Subwavelength Gratings for Polarization Pinning of Bottom-Emitting GaAs VCSELs

Erik Strandberg, *Member, IEEE*, Mindaugas Juodėnas, Alexander Grabowski, *Member, IEEE*, Åsa Haglund, *Member, IEEE*, and Anders Larsson, *Life Fellow, IEEE*

***Abstract*—We demonstrate bottom-emitting GaAs vertical-cavity surface-emitting lasers (VCSELs) incorporating a buried subwavelength grating in the top, highly reflective distributed Bragg reflector (DBR), with oxide aperture diameters ranging from 2 to 6. The buried grating successfully pins the polarization for aperture diameters up to 4 μm, and the 3 μm aperture VCSELs achieve single-mode, single-polarization operation, delivering 3.9 mW of output power with a side-mode suppression ratio exceeding 30 dB and an orthogonal polarization suppression ratio (OPSR) of 20 dB. Simulations and measurements indicate that the buried surface-etched grating can only weakly influence the lasing mode in the bottom-emitting configuration, thereby preventing polarization pinning of higher-order modes in larger-aperture VCSELs. The surface-etched gratings introduce minor degradation in threshold current, slope efficiency, and beam profile.**

***Index Terms*—Vertical-cavity surface-emitting laser, subwavelength gratings, monolithic integration, polarization pinning.**

I. Introduction

THE vertical-cavity surface-emitting laser (VCSEL) is today an ubiquitous device. The low threshold current, high efficiency, circular emission beam, excellent high-speed performance, and the possibility of packing the laser in dense 2D arrays have established the GaAs-VCSEL as one of the primary light sources for driving short-range sensing and short-reach fiber-optic communications [1]. Moreover, there exists a continuously expanding range of more demanding applications for the VCSEL, requiring a single-mode output in a fixed linear polarization at several milliwatts of power, such as for miniature gyroscopes [2], sensing [3], atomic clocks [4], optical computing [5], [6], medical diagnostics [7].

Received 6 March 2026; revised 25 May 2026; accepted 9 July 2026. Date of publication 16 July 2026; date of current version 5 August 2026. This work was supported by Knut and Alice Wallenberg Foundation under Grant 2020.0119, and the fabrication was performed in the Myfab cleanroom at Chalmers University of Technology in Gothenburg. *(Corresponding author: Erik Strandberg.)*

Erik Strandberg and Åsa Haglund are with the Department of Microtechnology and Nanoscience, Chalmers University of Technology, 412 96 Gothenburg, Sweden (e-mail: erik.strandberg@chalmers.se; asa.haglund@chalmers.se).

Mindaugas Juodėnas is with the Institute of Materials Science, Kaunas University of Technology, 514 23 Kaunas, Lithuania (e-mail: mindaugas.juodenas@ktu.lt).

Alexander Grabowski is with Solinide Photonics, 433 34 Partille, Sweden (e-mail: agrabowski@solinide.com).

Anders Larsson, retired, was a professor (e-mail: profandy57@gmail.com).

This article has supplementary material provided by the authors and color versions of one or more figures available at https://doi.org/10.1109/JSTQE.2026.3714146.

Digital Object Identifier 10.1109/JSTQE.2026.3714146

The polarization state in oxide-confined GaAs-VCSELs is generally unpredictable due to the material's weak anisotropy and the cavity's rotational symmetry. Every individual transverse mode of the VCSEL has a linear polarization state lying in the plane of the epitaxial layer. Due to the electro-optic effect, the electric field vector of the lasing modes is typically oriented along the $[011]$ or $[0\bar{1}1]$-crystallographic directions for a VCSEL grown on a (100) oriented GaAs substrate [8]. During VCSEL operation, changes in temperature, charge-carrier density, and optical feedback lead to competition between the two orthogonal states, resulting in an unpredictable polarization switching of the emitted beam. Pinning the polarization to a single linear state has been extensively studied through various modifications to the VCSEL cavity. The aim is to distinguish the lasing conditions between orthogonal polarization states by altering the waveguiding or by introducing anisotropic gain or loss. A common approach is to integrate or replace the DBR with subwavelength structures, such as surface-etched subwavelength gratings [9], surface-etched photonic crystals [10], subwavelength guided-mode resonance gratings [11], replacing the top DBR [12] or both DBRs with suspended high-contrast gratings [13]. Among these, the surface-etched subwavelength grating stands out due to its straightforward fabrication process [14], its ability to achieve a high orthogonal polarization suppression ratio (OPSR), and its minimal degradation of overall lasing performance

The subwavelength grating creates a layer with an anisotropic effective refractive index, which introduces different reflections from DBR for the two orthogonal polarization states. Depending on whether the reflections are in phase or out of phase with the optical standing wave, the result is either a low or a high overall modal loss. Thus, the state experiencing a higher loss will require a larger gain to reach the lasing threshold than the orthogonal state does. Moreover, the subwavelength grating has been demonstrated to pin the polarization along either the $[011]$ or $[0\bar{1}1]$ directions, overcoming unintentional weak anisotropies induced by operation, fabrication, or epitaxial growth. In addition, the transverse extent of a subwavelength grating can be used to radially vary the mirror reflectivity, thereby enabling higher single-mode output power with a pinned polarization state [15], [16], [17].

The most common VCSEL is top-emitting, with a lower reflective outcoupling DBR at the wafer surface. The opposite bottom-emitting VCSEL, as seen in Fig. 1, has not yet been as widely utilized, but can offer improved thermal management

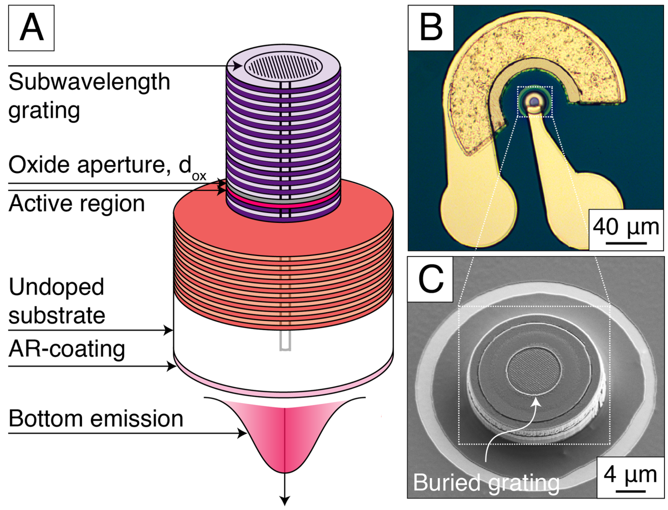

Fig. 1. (A) Schematic of the fabricated bottom-emitting VCSEL with a buried subwavelength grating for polarization pinning. The diameter of the oxide aperture, d_{ox}, sets the extent of the transverse waveguide and thereby the transverse mode distribution for the VCSEL. (B) Microscope image of the fully processed bottom-emitting polarization-pinned VCSEL. (C) SEM image of the VCSEL mesa with the buried subwavelength grating before the metallization of the probe pads.

due to fewer ternary layers between the active region and the substrate, as well as the possibility of integration via flip-chip bonding [18], [19]. Moreover, the substrate of the bottom-emitting VCSEL is well-suited for on-chip integration of micro- or metaoptics, leveraging the small footprint of the VCSEL to deliver an extremely compact laser source with a tailored on-chip beam profile [20], [21]. However, the bottom-emitting VCSEL has a highly reflective DBR ($> 99.9\%$) at the wafer surface. This implies that a surface-etched subwavelength grating will interact less strongly with the lasing modes since the optical field intensity at the surface is lower than in a top-emitting VCSEL. The low optical intensity has led to the development of alternative techniques to pin the polarization of the bottom-emitting VCSEL, such as depositing a metal grating on the top DBR [22], [23], or deeply etched grooves in the vicinity of the VCSEL mesa [24]. However, these techniques exhibit low OPSR or an inability to pin the polarization to either orthogonal state, suggesting that they can only weakly affect the lasing mode.

The driving factor for pinning the polarization state with the subwavelength grating is the induced difference in modal cavity loss between the two orthogonal polarization states. For the top-emitting GaAs-VCSEL, a typical difference reaches $\Delta\alpha_{\text{loss}} > 20\ \text{cm}^{-1}$, depending on the epitaxial structure and grating parameters [17], [25]. In comparison, the fabricated bottom-emitting VCSELs for this demonstration showed a maximum modal cavity loss difference of $\Delta\alpha_{\text{loss}} = 10.4\ \text{cm}^{-1}$. Here, we demonstrate that, despite this lower loss difference, the subwavelength grating can effectively pin the polarization for aperture diameters up to $4\ \mu\text{m}$, with a minor degradation in the lasing performance. Moreover, the polarization pinning remains robust after burying the grating, which is important for protecting the VCSEL during integration of micro- or metaoptics in the bottom-emitting device substrate.

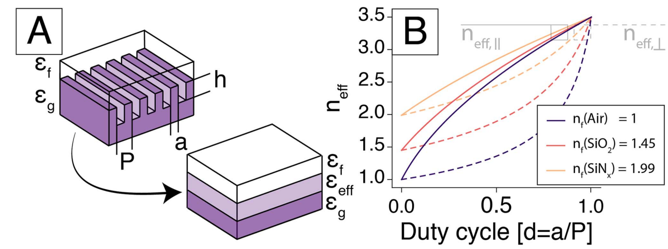

Fig. 2. (A) Schematic of the effective permittivities used in the simulations for the buried subwavelength grating. The duty cycle is defined as the grating ridge-to-period ratio, $d = a/P$. (B) Effective refractive index of the subwavelength grating according to (1). The lasing modes will experience different refractive indices depending on whether the electric field is parallel (filled lines) or perpendicular (dashed lines) to the grating lines.

II. Polarization-Pinned VCSEL Design

A. Subwavelength Grating Simulations

To design the subwavelength grating, cold-cavity simulations were performed with the well-known effective index method [26], [27] with refractive index data for the $Al_xGa_{1-x}As$ layers from the Afromowitz model [28]. The gratings were designed with a subwavelength periodicity, $P = 260$ nm, which eliminates all nonzero diffraction orders in both transmission and reflection. In Fig. 2(A), the schematic of the grating parameters and the effective permittivities of the layers used to simulate the grating are presented.

Since the wavelength is larger than the grating period, it interacts with the grating as if it were a medium with an anisotropic effective permittivity. This can be estimated analytically using the boundary conditions and spatial weighting of the electric and displacement fields, as

$$\epsilon_{||} = d\epsilon_{\text{g}} + (1-d)\epsilon_{\text{f}}, \quad \epsilon_{\perp} = \frac{\epsilon_g \epsilon_{\text{f}}}{d\epsilon_{\text{f}} + (1-d)\epsilon_{\text{g}}}, \qquad (1)$$

where $\epsilon_{||}$ and $\epsilon_{\perp}$ are the permittivities experienced by an electric field parallel or perpendicular to the grating lines, respectively [29]. ϵ_g is the permittivity of the grating ridge, ϵ_{f} is the permittivity of the material filling the grooves of the grating, and d is the duty cycle of the grating, defined as the ridge-to-period ratio, $d = a/P$.

The effective anisotropic refractive index of the grating layer from (1) is shown in Fig. 2(B) as a function of duty cycle for the grating. In addition, to the unburied grating, with air in the grooves ($n_f = 1$), Fig. 2(B), it also presents the anisotropic index when SiO_2 ($n_{\text{f}} = 1.45$), and SiN_x ($n_{\text{f}} = 1.99$) are filling the grating's grooves. The refractive index of the dielectric films was determined by ellipsometry at $\lambda = 980$ nm, the designed lasing wavelength for the fabricated VCSELs. As shown, the contrast in refractive index between the orthogonal states can be tailored by the duty cycle of the grating. When the field is parallel to the grating lines, the refractive index is relatively high, closer to the grating medium. Whereas, for the perpendicular case, it is lower, closer to the index of the material in the grooves of the grating. As a consequence, the refractive-index contrast between the states is significantly reduced when the grating is filled with a material that has a refractive index between air and that of the grating, such as SiN_x or SiO_2.

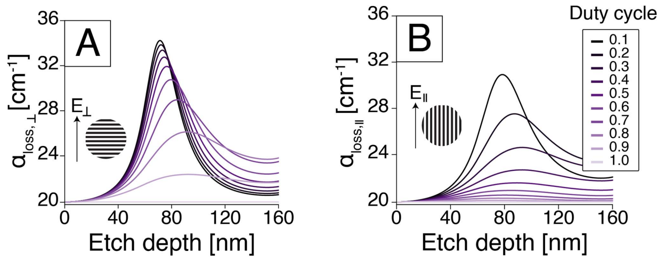

Fig. 3. The simulated modal cavity loss as a function of the grating etch depth, h, and the duty cycle of the grating, d, for the modes with an electric field (A) perpendicular to the grating lines, and (B) parallel to the grating lines. The simulation for a grating with air in the grooves, $n_f = 1$.

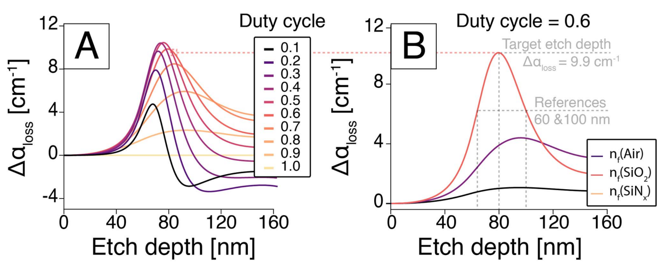

Fig. 4. Difference in modal cavity loss simulations as a function of the grating etch depth, h, and the grating duty cycle, d. (A) Shows the difference in modal cavity loss across all duty cycles when the grating grooves are filled with air ($n_f = 1$). (B) Shows the difference in modal cavity loss for the duty cycle, $d = 0.6$, when the grating grooves are filled with air, ($n_f = 1$), SiO_2 ($n_f = 1.45$), and SiN_x ($n_f = 1.99$).

Fig. 3 presents the simulated cold-cavity modal losses, α_{loss}, as a function of the grating etch depth, h, and the duty cycle, d. In Fig. 3(A) the modal cavity loss is seen for the state with the electric field perpendicular to the grating lines, $\alpha_{loss,\perp}$, and in Fig. 3(B) the modal cavity losses for the state with the electric field parallel to the grating lines, $\alpha_{loss,\parallel}$. The increase in modal cavity losses is due to reflections from the etched grating. Without the grating, the DBR is designed to produce constructive interference from all the partial reflections at all the interfaces of the epitaxial DBR. When the grating is etched down, it induces new reflections that are out of phase, thereby decreasing the total reflectance of the mirror and, in turn, increasing the modal losses. The maximum modal cavity loss occurs when the grating is etched to a depth such that the resulting reflection is antiphase with the optical standing wave, the same effect as if one layer of the DBR pair were etched away. In addition, the maximum in modal cavity loss or the antiphase reflection occurs at shallower etch depths for smaller duty cycles, shown in Fig. 3, since the lower refractive index, from Fig. 2(B), results in a larger phase shift relative to the unetched DBR (see Supplementary section 1 for details on the reflections from the grating).

In Fig. 4(A) the difference in the modal cavity between the orthogonal states, $\Delta\alpha_{loss} = \alpha_{loss,\perp} - \alpha_{loss,\parallel}$, is shown as a function of the grating parameters for unburied grating with air in the grooves, $n_f = 1$. Due to the low optical intensity at the surface in the bottom-emitting configuration, the maximum difference in modal cavity loss reaches $\Delta\alpha_{loss} = 10.4\ cm^{-1}$ for the duty cycle, $d = 0.5$. Since the modal losses introduced by the grating are lower for the parallel state, it is the favored state for lasing and the state to which the VCSEL emission will be pinned. Moreover, as seen in Fig. 3(B), the modal cavity loss is also significantly increased for the parallel state with a smaller duty cycle. In contrast to the top-emitting VCSEL, the slope efficiency of the bottom-emitting VCSEL does not increase with the grating, since the increase in modal loss is primarily due to increased mirror loss in the top mirror caused by the grating. Thus, the modal loss of the parallel state should be kept as low as possible to minimize the impact on the bottom-emitting VCSEL's performance (see Supplementary section 2 for full simulation details).

It has been experimentally estimated, by placing a VCSEL in a T-shaped external cavity, that a difference of $\Delta\alpha_{loss} \approx 10\ cm^{-1}$ is sufficient to pin the polarization [30]. Therefore, the duty cycle of $d = 0.6$ was selected for the gratings, as presented in Fig. 4(B). With an etch depth of $h = 80$ nm, the grating achieves the relatively large difference in modal cavity loss, $\Delta\alpha_{loss} = 9.9\ cm^{-1}$. Simultaneously, it keeps the modal cavity loss low for the pinned parallel state, $\alpha_{loss,\parallel} = 20.9\ cm^{-1}$, which is a minor increase, $0.96\ cm^{-1}$, compared to an unetched VCSEL. In addition, Fig. 4(B), shows the significant reduction in the difference if the modal cavity loss, where SiO_2 ($n_f = 1.45$), or SiN_x ($n_f = 1.99$), fills the grooves of the grating. Moreover, since the difference in modal cavity loss is relatively small compared to that of the top-emitting VCSEL, $\Delta\alpha_{loss} > 20\ cm^{-1}$, we assessed the pinning strength and fabrication tolerance of the buried gratings by fabricating additional VCSELs with shallower and deeper etched gratings ($h = 60$ and 100 nm, respectively) for reference, as seen in Fig. 4(B).

B. VCSEL and Subwavelength Grating Fabrication

The fabricated bottom-emitting VCSEL consists of a 1λ-cavity formed by two epitaxially grown DBRs, sandwiching an active region with multiple InGaAs QWs designed to lase at $\lambda = 980$ nm. The top p-doped DBR consists of 28 mirror pairs of $GaAs/Al_{0.90}Ga_{0.10}As$ and the bottom n-doped DBR consists of 3 $GaAs/Al_{0.90}Ga_{0.10}As$ + 18 AlAs/GaAs mirror pairs, with graded-composition interfaces and modulation doping to minimize electrical resistance. A microscope image of the fabricated VCSEL is shown in Fig. 1(B), as well as a SEM image of the VCSELs with the buried subwavelength grating in Fig. 5(A) (see Supplementary section 3 for details on the epitaxial layers and fabrication of the VCSELs).

The VCSELs are oxide confined, via a 20-nm-thick $Al_{0.985}Ga_{0.015}As$ layer in the top DBR. The significantly higher aluminum content (98.5%) enables selective wet oxidation to form an oxide aperture. The diameter of the formed aperture, d_{ox}, is arguably the most significant parameter in the fabrication of an oxide-confined VCSEL, since it determines the transverse mode distribution and overall laser performance. In addition, the fabricated VCSELs are referred to as weakly guided since the oxide aperture is placed at a node of the optical standing wave, resulting in the small effective index step, $\Delta n_{eff} = 0.000352$, of the waveguide. Weak guiding enables the largest possible aperture that only supports the fundamental transverse mode, yielding the highest output power in single-mode operation.

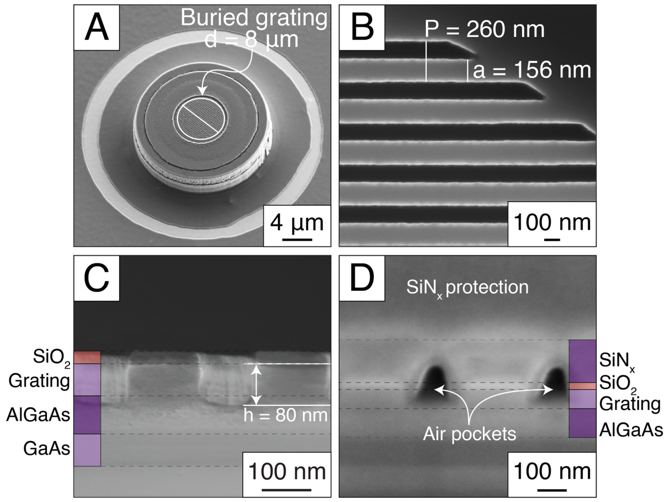

Fig. 5. (A) SEM image of the fabricated VCSELs with a buried subwavelength grating before the metallization of the probe pads. The image shows a VCSEL with oxide aperture diameter, $d_{ox} = 2\,\mu m$, with the corresponding grating diameter, $d_{grating} = 8\,\mu m$. (B) SEM image of the etched subwavelength grating atop the VCSEL mesa before deposition of SiN_x. (C) SEM image of the cross-section of the etched grating. **D)** SEM imagee of the cross-section of a focused ion-beam etched VCSEL mesa, tilted at 70°. The cross-section shows that air pockets form along the grating lines after burying the grating in SiN_x, thereby maintaining a high refractive index between the grating ridge and groove.

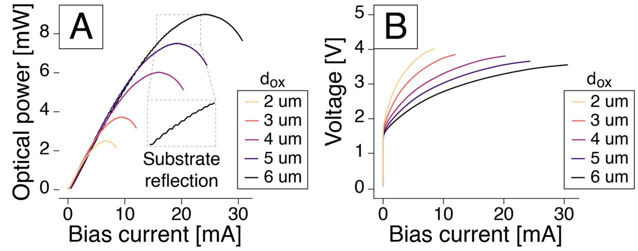

Fig. 6. Current-power-voltage (IPV) measurements for $d_{ox} = 2\text{-}6\,\mu m$ VCSELs with integrated buried subwavelength gratings. (A) Optical output power as a function of the bias current. The inset shows the ripple in the output power due to the back reflection from the substrate. (B) The corresponding voltage as a function of the bias current.

The VCSEL cavity was grown on an undoped substrate to minimize free-carrier absorption of the emitted beam as it propagates through the substrate. In addition, a $\lambda/4$ anti-reflective SiN_x coating was deposited at the bottom of the substrate to reduce the optical feedback to the cavity from the GaAs-air interface.

Before the etching of the VCSEL mesa, the subwavelength grating was integrated in the top surface of the highly reflective DBR. As shown in Fig. 5(A) the grating covers the mesa to the edge of the metalized ring contact. The diameter of the integrated gratings was $6\,\mu m$ larger than the oxide aperture diameter of the VCSEL, as illustrated in Fig. 5(A) by a $2\,\mu m$ oxide aperture VCSEL with the corresponding $8\,\mu m$ diameter grating. The large grating diameter, relative to the aperture, was intentional so as not to affect the transverse waveguiding of the VCSEL. The subwavelength grating was fabricated by sputtering a 100-nm-thick SiO_2 film and patterning AR-P 6200 resist by electron-beam lithography (EBL). The pattern was transferred into the SiO_2 with a CF_4-O_2 reactive ion etch, followed by etching the grating into the AlGaAs layers of the DBR with a switched Ar-$SiCl_4$ and O_2 reactive ion etch with an inductively coupled plasma [31]. Fig. 5(B) shows an SEM image of the top view of the etched subwavelength gratings atop the VCSEL mesa before they are buried in SiN_x. The sidewall roughness, seen in Fig. 5(C), on the grating ridges was caused by scallops due to the switched etching process. However, sidewall roughness has a negligible effect on the anisotropic effective refractive index needed for the polarization pinning (see Supplementary section 4 for fabrication details).

As described in the previous section, the maximum difference in modal cavity loss, $\Delta\alpha_{loss}$, was achieved with the grating depth $h = 80$ nm, as seen in Fig. 4(A), for an unburied grating air in the grooves of the grating. Since etching 80 nm, exposes the second DBR layer, with a high aluminum content $Al_{0.9}Ga_{0.1}As$, the subwavelength grating was buried in a thick layer of sputtered SiN_x to protect it from the subsequent aperture oxidation. In addition, burying the grating protects it from any further substrate fabrication. Since the difference in modal cavity losses is drastically reduced by filling the grating with a higher refractive index material, as seen in Fig. 4(B), the protective SiN_x was sputtered onto the SiO_2 etching mask, forming air pockets along the grating lines. This maintains the high refractive index contrast between GaAs and air in the grating region. To verify the presence of air along the grating lines, the VCSEL mesa with a buried subwavelength grating was cut using focused-ion-beam etching. Fig. 5(D) shows the cross-section of the cut mesa, tilted at 70°, where teardrop-shaped air-pockets along the grating grooves can be seen.

III. Polarization-Pinned VCSEL Performance

A. *Polarization-Resolved Current-Power-Voltage Characteristics*

The light emitted by the bottom-emitting VCSELs was collected by an integrating sphere (Ophir IS6-D-UV) placed 1 cm from the substrate surface, close enough to capture the entire divergent beam. The emission from either polarization state was measured as a function of the bias current by inserting a linear polarizer in front of the integrating sphere. The OPSR was calculated as $\mathrm{OPSR} = 10\log\left(\frac{P_{||}}{P_{\perp}}\right)$, where $P_{||}$ and $P_{\perp}$ are the optical power from the mode with an electric field parallel and perpendicular to the grating lines, respectively. Fig. 6 shows the current-power-voltage (IPV) measurements for the full range of oxide aperture diameters examined, $d_{ox} = 2\text{–}6\,\mu m$. The ripple evident in all measurements, seen magnified in the inset of Fig. 6(A), was attributed to back reflection from the GaAs-SiN_x -air interface at the bottom of the substrate with an estimated residual power reflectivity of about 3%. In Fig. 7 the polarization-resolved current-power (PRIP) measurements can be seen for gratings aligned with either of the polarization states for VCSELs with 3 and $4\,\mu m$ aperture diameters. In Fig. 7(A) and (B) the grating pins the polarization state in the [011]-crystallographic direction, and Fig. 7(C) and (D) to the

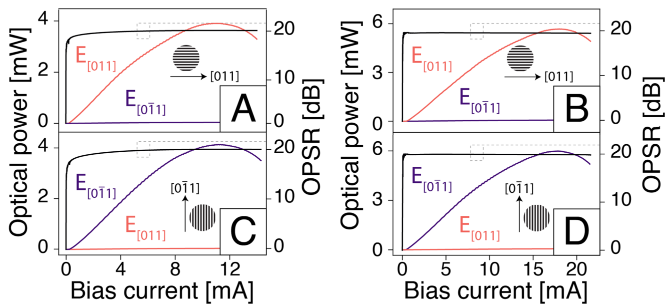

Fig. 7. Polarization resolved current-power (PRIP) measurements for the VCSELs with a pinned polarization. **A, B)** PRIP measurements when the grating lines are aligned with [011]-crystallographic direction for the 3 and 4 μm aperture VCSELs. **C, D)** PRIP measurements when the grating lines are aligned with the perpendicular $[0\bar{1}1]$-direction for the 3 and 4 μm aperture VCSELs. Depending on the grating orientation, the polarization can be pinned to either polarization state over the entire biasing range with OPSR= 20 dB.

orthogonal $[0\bar{1}1]$-direction. The VCSELs with a pinned polarization achieve OPSR ≈ 20 dB over the entire biasing range, limited by unpolarized spontaneous emission from the VCSEL and ambient noise.

For devices with larger apertures, 5–6 μm, the polarization undergoes at least one switch between threshold and thermal rollover. This instability is due to the larger waveguides supporting higher-order transverse modes, which exhibit greater angular divergence than the fundamental mode. Because the effective anisotropic index of the grating is angle-dependent, this increased divergence diminishes the index contrast between the parallel and perpendicular polarization states. As a result, the differential modal cavity loss for higher-order modes is reduced, preventing the polarization pinning. Additionally, the 1D effective-index simulations of modal cavity loss, shown in Fig. 4(A), assume a perfectly vertical plane wave with no transverse wavevector components, $k_{\perp} = 0$. Therefore, the 1D model overestimates the modal cavity losses for higher-order modes, which are composed of a broader range of transverse wavevectors due to their increased divergence (see Supplementary section 5 for the polarization instability of the higher-order modes).

Moreover, the VCSELs with etched gratings at shallower ($h = 60$ nm) and deeper ($h = 100$ nm) depths exhibited an unpredictable polarization state across the examined aperture sizes. Consequently, the mirror-loss difference, $\Delta\alpha = 9.9\,\mathrm{cm}^{-1}$, achieved by the $h = 80$ nm deep grating lies at the boundary for pinning the polarization. In addition, filling the surface-etched gratings completely with a higher-refractive-index film, such as SiO_2 or SiN_x, would not create a large enough anisotropy to pin the polarization, as seen in Fig. 4(B). (see Supplementary section 6 for polarization switching details)

B. Spectral Characteristics

The VCSEL spectra were measured with an optical spectrum analyzer (Yokogawa AQ6317 C) as a function of bias current. The OSA resolution was 0.1 nm, and all spectra are normalized to the maximum power measured at each bias current. Fig. 8 presents the spectra for the VCSELs with 3 and 4 μm aperture

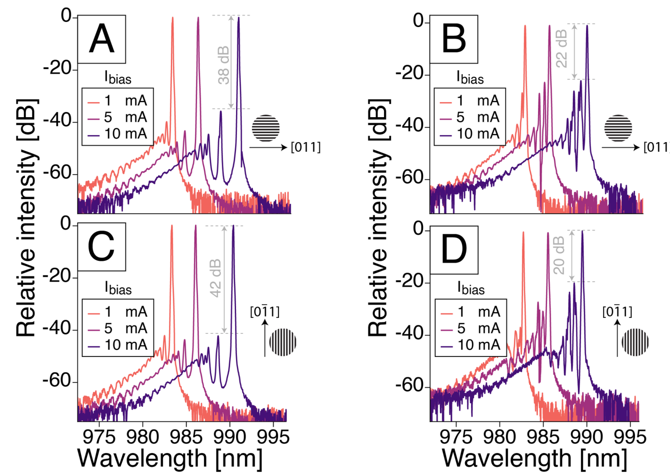

Fig. 8. Spectrum of the polarization-pinned VCSELs. **A, B)** Spectrum when the gratings lines are aligned with [011]-crystallographic direction for the 3 and 4 μm aperture VCSELs. **C, D)** Spectrum when the gratings lines are aligned with the $[0\bar{1}1]$-direction for the 3 and 4 μm aperture VCSELs. All spectra are normalized to the maximum power at each bias current. The suppression of higher-order modes exceeds 30 dB across the entire biasing range for the 3 μm VCSELs.

diameters, with a pinned polarization. Fig. 8(A) and (B) shows the typical spectrum for a 3 and the 4 μm aperture VCSELs with the polarization pinned to the [011]-crystallographic direction. Similarly, Fig. 8(C) and (D), presents the typical spectrum for the 3 and the 4 μm VCSELs with the polarization pinned to the perpendicular $[0\bar{1}1]$ -direction. For the 3 μm aperture, the emission is considered quasi single-mode, as the side-mode suppression ratio (SMSR) exceeded 30 dB across the entire biasing range. The 3 μm aperture VCSELs were the largest aperture operating in single mode and reached a maximum output power of $P_{\mathrm{max}} = 3.9$ mW, seen in the PIPV from Fig. 7(A) and (B). At lower bias currents, the 4 μm aperture achieves a side-mode suppression ratio exceeding 30 dB. However, as the bias current was increased, higher-order modes contributed significantly to the output power, reducing the side-mode suppression ratio. The 4 μm aperture VCSELs reached an OPSR ≈ 20 dB despite the presence of multiple transverse modes, with a maximum output power of $P_{\mathrm{max}} = 6.0$ mW, as shown in Fig. 7(C) and (D). The smaller redshift of the fundamental mode with increasing bias current, observed in the 4 μm aperture, is due to a smaller temperature increase resulting from the lower differential resistance of the larger aperture.

C. Far-Field Characteristics

The far-fields were captured by illuminating a diffuse screen (Ophir WB-I SWIR) and imaging it onto a CCD camera (Ophir SP932 U). To average out the spatial speckle arising from coherent illumination of the diffusive plate, all presented far fields are averages of 10 measurements with slightly varied bias currents, $\Delta I_{\mathrm{b}} = \pm 0.05$ mA. In Fig. 9(A) a line profile of the far-field for the 3 μm VCSEL with the polarization pinned to the [011]-crystallographic direction is presented over the full biasing range, with an inset of a cross-section at bias current 1 mA. The divergence angle was measured to 26.6° ($1/e^2$ -full width) at

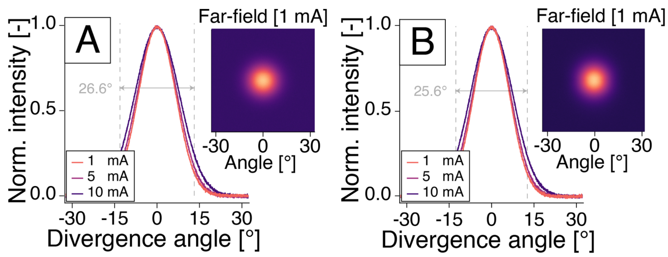

Fig. 9. (A) Line section of the far-field emission for the polarization-pinned 3 µm VCSEL, with an inset a cross-section of the far-field at 1 mA. (B) Similarly, shows a line section with an inset showing the far-field cross-section at 1 mA for the 4 µm VCSEL. The far-fields show that the subwavelength grating does not distort the emitted beam.

1 mA, which corresponds to a beam waist of 2.6 µm in the active region of the VCSEL and a beam width of 83.1 µm ($1/e^2$-full width) at the bottom GaAs-SiN_x-air interface. The divergence angle increased to 31.2° when the current was increased to 10 mA, due to thermal lensing. In Fig. 9(B) a line profile of the far-field for the 4 µm VCSEL, with the polarization pinned to the [011]-crystallographic direction, is presented over the full biasing range, with an inset of the cross-section of the far-field at bias current 1 mA. The divergence angle was measured to 25.6° ($1/e^2$-full width) at 1 mA. The far-fields from both the 3 and 4 µm show that the subwavelength grating does not distort the emitted beam, as it does not introduce side lobes.

D. Subwavelength Grating Influence on Lasing Characteristics

To investigate the impact of the subwavelength grating on lasing performance, we measured five VCSELs with integrated gratings, pinning the polarization to either the [011] or $[0\bar{1}1]$ directions, alongside five unetched reference VCSELs across the aperture range 2–6 µm. The extracted lasing characteristics, threshold current, slope efficiency, and maximum output power, are summarized in Fig. 10. The threshold current was identified as the bias current at which the output power exhibited a distinct kink. The slope efficiency was determined by the slope of the optical power, from threshold to half the maximum output power. The maximum output power was measured at the thermal rollover point.

As illustrated in Fig. 10, the integration of the subwavelength grating resulted in a minor degradation across the measured lasing characteristics. The variance of the oxide aperture diameter in Fig. 10 is attributed to the oxidation rate gradient across the fabricated chip. As seen in Fig. 10(A), the minor increase in threshold current for the VCSELs with the gratings was anticipated, given the estimated increase in modal cavity loss, 0.96 cm^{-1}, for the pinned polarization state with electric field parallel to the grating lines, Fig. 3(B). In Fig. 10(B), the increased losses from the highly reflective top mirror do not enhance slope efficiency for the bottom-emitting VCSELs, in contrast with top-emitting VCSELs, since light is extracted through the substrate. The minor reduction of the slope efficiency is also due to the small increase in modal cavity loss for the pinned polarization state. As seen in Fig. 10(C), the combination of a

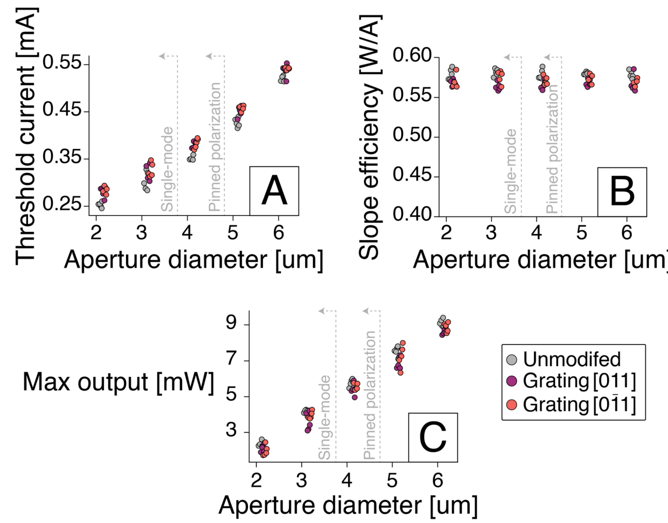

Fig. 10. Summary of lasing characteristics for VCSELs with and without subwavelength gratings. For each aperture diameter, five reference devices and five devices with gratings aligned along the [011] and $[0\bar{1}1]$ directions were measured. (A) Threshold current, (B) slope efficiency, and (C) maximum output power versus oxide aperture diameter.

higher threshold current and a reduced slope efficiency leads to a lower maximum output power.

IV. Discussion

Experimental results and supporting simulations demonstrate that buried surface-etched subwavelength gratings within the highly reflective top DBR effectively pin the polarization state in bottom-emitting GaAs-VCSELs. This pinning was observed for oxide apertures up to 4 µm using a grating depth of 80 nm, confirming that sufficient anisotropy was achieved despite the low optical intensity at the top surface. However, devices with 60-nm and 100-nm grating depths exhibited unpredictable polarization states. This indicates that the influence of the grating is relatively weak, resulting in a minimum fabrication tolerance of ±20 nm. To relax these tolerances and enhance pinning strength, the first mirror layer of the top DBR could be blank-etched prior to grating fabrication, thereby increasing the optical field intensity at the surface and increasing the interaction with the grating. However, the increased losses from the top mirror will come with a larger penalty to the VCSEL performance. Another approach to relax the fabrication tolerance is to design the epitaxial structure so that the outermost DBR layer initially provides an antiphase reflection and then etching down the polarization-pinning grating [17]. In addition, by increasing interaction with the subwavelength grating, the system could be combined with a spatial-mode filter to further increase single-mode output power by selectively increasing the cavity loss for higher-order transverse modes.

An alternative approach involves forming an external cavity by integrating a metasurface to design the optical feedback from the substrate side [32]. Given the high degree of freedom metasurfaces offer in tailoring the shape and polarization state of a beam, this method can simultaneously pin the polarization and enhance mode selectivity [33]. Nevertheless, fabricating a single metasurface to manage cavity feedback, pinning the VCSEL polarization state, and simultaneously shaping the transmitted beam into a desired profile poses a significant design and fabrication challenge.

From a fabrication perspective, while electron-beam lithography provides excellent dimensional control for defining subwavelength gratings, its high cost and limited throughput make it unsuitable for large-scale production. Nanoimprint lithography presents an attractive alternative, offering nanometer-scale resolution at the wafer scale [14]. Furthermore, to maximize the difference in modal cavity losses, a high GaAs/air index contrast could be achieved by etching the grating after oxidation or by removing the protective film after VCSEL fabrication. However, this approach would require an additional form of protection for the top surface during any subsequent backside processing. Therefore, the buried surface-etched grating provides a highly practical alternative for polarization control when integrating micro-optics or metasurfaces on the substrate side of a bottom-emitting VCSEL. The minor degradation observed in threshold current, slope efficiency, and beam quality indicates that the induced anisotropy primarily affects polarization, leaving the backside pristine for integration with these nano- or metaoptics.

V. Conclusion

We experimentally demonstrate polarization control in 980 nm oxide-confined, bottom-emitting VCSELs utilizing a buried subwavelength grating etched into the highly reflective top mirror. The grating induces polarization-dependent modal cavity loss, effectively pinning the VCSEL into a state parallel to the grating lines. For devices with a 3 μm oxide aperture, single-mode operation was achieved with a side-mode suppression ratio (SMSR) exceeding 30 dB, an orthogonal polarization suppression ratio (OPSR) of approximately 20 dB, and an optical output power up to 3.9 mW. At a 4 μm aperture diameter, polarization was successfully pinned to either orthogonal state, with output powers reaching 6 mW, though with a reduced SMSR of $\approx$20 dB. In devices with apertures exceeding 4 μm, the grating-induced threshold gain difference is insufficient to maintain pinning, resulting in at least one polarization switch before thermal rollover. Finally, the buried gratings provide a straightforward fabrication route to polarization-stable VCSELs with minimal degradation in threshold current and output power. Crucially, this platform leaves the substrate pristine, enabling monolithic integration with on-chip optical metasurfaces for advanced spatial beam shaping and mode-selective photonic applications.

Acknowledgment

The authors acknowledge Artem Shushanian at Chalmers University of Technology for assistance with focused-ion-beam cutting. This paper was produced by the IEEE Publication Technology Group. They are in Piscataway, NJ.

References

[1] A. Larsson, “Advances in VCSELs for communication and sensing,” *IEEE J. Sel. Topics Quantum Electron.*, vol. 17, no. 6, pp. 1552–1567, Nov./Dec. 2011.

[2] Y. Zhou et al., “Large-aperture single-mode 795 nm VCSEL for chip-scale nuclear magnetic resonance gyroscope with an output power of 4.1 mW at 80°C,” *Opt. Exp.*, vol. 30, no. 6, Mar. 2022, Art. no. 8991.

[3] A. Liu, P. Wolf, J. A. Lott, and D. Bimberg, “Vertical-cavity surface-emitting lasers for data communication and sensing,” *Photon. Res.*, vol. 7, no. 2, pp. 121–136, Feb. 2019.

[4] M. Huang, D. K. Serkland, and J. Camparo, “A narrow-linewidth three-mirror VCSEL for atomic devices,” *Appl. Phys. Lett.*, vol. 121, no. 11, Sep. 2022, Art. no. 114002.

[5] T. Heuser et al., “Developing a photonic hardware platform for brain-inspired computing based on 5 VCSEL arrays,” *J. Phys.: Photon.*, vol. 2, no. 4, Oct. 2020, Art. no. 044002.

[6] “Deep learning with coherent VCSEL neural networks,” *Nature Photon.*, vol. 17, no. 8, pp. 723–730, Aug. 2023.

[7] M. Kendrisic et al., “Thermally tuned VCSEL at 850 nm as a low-cost alternative source for full-eye SS-OCT,” *Opt. Lett.*, vol. 48, no. 11, Jun. 2023, Art. no. 3079.

[8] R. Michalzik, Ed., *VCSELs: Fundamentals, Technology and Applications of Vertical-Cavity Surface-Emitting Lasers (Springer Series in Optical Sciences Series)*, vol. 166. Berlin, Germany: Springer, 2013.

[9] P. Debernardi, J. Ostermann, M. Feneberg, C. Jalics, and R. Michalzik, “Reliable polarization control of VCSELs through monolithically integrated surface gratings: A comparative theoretical and experimental study,” *IEEE J. Sel. Topics Quantum Electron.*, vol. 11, no. 1, pp. 107–116, Jan./Feb. 2005.

[10] K.-H. Lee et al., “Square-lattice photonic-crystal vertical-cavity surface-emitting lasers,” *Opt. Exp.*, vol. 12, no. 17, 2004, Art. no. 4136.

[11] L.-S. Fu et al., “Subwavelength-grating coupled-cavity resonance VCSELs with ultra-narrow linewidth,” *APL Photon.*, vol. 10, no. 5, May 2025, Art. no. 056112.

[12] M. C. Huang, Y. Zhou, and C. J. Chang-Hasnain, “A surface-emitting laser incorporating a high-index-contrast subwavelength grating,” *Nature Photon.*, vol. 1, no. 2, pp. 119–122, Feb. 2007.

[13] M. Gebski, M. Dems, M. Wasiak, J. A. Lott, and T. Czyszanowski, “Monolithic subwavelength high-index-contrast grating VCSEL,” *IEEE Photon. Technol. Lett.*, vol. 27, no. 18, pp. 1953–1956, Sep. 2015.

[14] M. Grabherr et al., “Volume production of polarization controlled single-mode VCSELs,” *Proc. SPIE*, vol. 6908, Feb. 2008, Art. no. 690803.

[15] P. Debernardi et al., “Single-mode, single-polarization VCSELs via elliptical surface etching: Experiments and theory,” *IEEE J. Sel. Topics Quantum Electron.*, vol. 9, no. 5, pp. 1394–1404, Sep./Oct. 2003.

[16] M. C. Y. Huang, Y. Zhou, and C. J. Chang-Hasnain, “Single mode high-contrast subwavelength grating vertical cavity surface emitting lasers,” *Appl. Phys. Lett.*, vol. 92, no. 17, Apr. 2008, Art. no. 171108.

[17] A. Haglund, J. Gustavsson, J. Bengtsson, P. Jedrasik, and A. Larsson, “Design and evaluation of fundamental-mode and polarization-stabilized VCSELs with a subwavelength surface grating,” *IEEE J. Quantum Electron.*, vol. 42, no. 3, pp. 231–240, Mar. 2006.

[18] C.-K. Lin, A. Tandon, K. Djordjev, S. W. Corzine, and M. R. T. Tan, “High-speed 985 nm bottom-emitting VCSEL arrays for chip-to-chip parallel optical interconnects,” *IEEE J. Sel. Topics Quantum Electron.*, vol. 13, no. 5, pp. 1332–1339, Sep./Oct. 2007.

[19] M. Johnson, D. Siriani, P. Leisher, and K. Choquette, “In-phase antiguided bottom-emitting vertical cavity laser arrays,” *Electron. Lett.*, vol. 49, no. 14, pp. 897–898, Jul. 2013.

[20] G. Pan et al., “Harnessing the capabilities of VCSELs: Unlocking the potential for advanced integrated photonic devices and systems,” *Light: Sci. Appl.*, vol. 13, no. 1, Sep. 2024, Art. no. 229.

[21] B. Wu et al., “Directional perfect poincaré beams generated by spin-decoupling of VCSELs using integrated metasurfaces,” *Nano Lett.*, vol. 25, no. 38, pp. 14002–14009, Sep. 2025.

[22] T. Mukaihara et al., *IEEE J. Sel. Topics Quantum Electron.*, vol. 1, no. 2, pp. 667–673, Jun. 1995.

[23] X. W. Zhang, Y. Q. Ning, L. Qin, Y. Liu, and L. J. Wang, “The design and analysis of sub-wavelength metal-grating large-aperture VCSELs,” *Appl. Phys. B*, vol. 109, no. 1, pp. 171–175, Oct. 2012.

[24] D. Lei, D.-H. Kim, N. Babazadeh, D. T. D. Childs, and R. A. Hogg, “Polarization-pinning in substrate emission multi-mode vertical-cavity surface-emitting lasers using deep trenches,” *Appl. Phys. Lett.*, vol. 120, no. 21, May 2022, Art. no. 211102.

[25] J. M. Ostermann et al., "Surface gratings for polarization control of single- and multi-mode oxide-confined vertical-cavity surface-emitting lasers," *Opt. Commun.*, vol. 246, no. 4-6, pp. 511–519, Feb. 2005.
[26] G. R. Hadley, "Effective index model for vertical-cavity surface-emitting lasers," *Opt. Lett.*, vol. 20, no. 13, Jul. 1995, Art. no. 1483.
[27] G. Hadley et al., "Comprehensive numerical modeling of vertical-cavity surface-emitting lasers," *IEEE J. Quantum Electron.*, vol. 32, no. 4, pp. 607–616, Apr. 1996.
[28] M. A. Afromowitz, "Refractive index of $\mathrm{Ga}_{1-x}\mathrm{Al}_x\mathrm{As}$," *Solid State Commun.*, vol. 15, no. 1, pp. 59–63, Jul. 1974.
[29] E. Hecht, *Optics*, 5th ed. London, U.K.: Pearson, 2017.
[30] D. Kuksenkov and H. Temkin, "Polarization related properties of vertical-cavity surface-emitting lasers," *IEEE J. Sel. Topics Quantum Electron.*, vol. 3, no. 2, pp. 390–395, Apr. 1997.
[31] M. Juodėnas et al., "High-angle deflection of metagrating-integrated laser emission for high-contrast microscopy," *Light: Sci. Appl.*, vol. 12, no. 1, Oct. 2023, Art. no. 251.
[32] L. Xu et al., "Metasurface external cavity laser," *Appl. Phys. Lett.*, vol. 107, no. 22, Nov. 2015, Art. no. 221105.
[33] X. Jia et al., "Metasurface reflector enables room-temperature circularly polarized emission from VCSEL," *Optica*, vol. 10, no. 8, Aug. 2023, Art. no. 1093.

Erik Strandberg (Member, IEEE) received the M.Sc. degree in engineering physics from the Chalmers University of Technology, Göteborg, Sweden, in 2021. He is currently working toward the Ph.D. degree with the Department of Microtechnology and Nanoscience, Chalmers. He is working on the monolithic integration of meta- and nanostructures into bottom-emitting GaAs-based vertical-cavity surface-emitting lasers (VCSELs), with a focus on their application in miniaturized biophotonics.

Mindaugas Juodėnas received the M.Sc. and Ph.D. degrees in material science from the Kaunas University of Technology, Kaunas, Lithuania, in 2017 and 2021, respectively. His main topic has been the fabrication and study of surface lattice resonances in self-assembled plasmonic lattices. He was a Postdoc with Chalmers University, where he worked on the monolithic integration of dielectric metasurfaces with GaAs vertical-cavity surface-emitting lasers (VCSELs) for biophotonics, focusing on the fabrication of GaAs metagrating for efficient light deflection. He is currently a Senior Researcher with the Kaunas University of Technology, working on dielectric metasurfaces for high power laser applications.

Alexander Grabowski (Member, IEEE) received the M.Sc. degree in electrical engineering and the Ph.D. degree from the Chalmers University of Technology, Göteborg, Sweden, in 2017 and 2022, respectively. His doctoral research focused on modeling of GaAs-based vertical-cavity surface-emitting lasers (VCSELs) for high-speed short-reach optical interconnects, as well as fabrication of GaAs-based VCSELs for micro-transfer-printing integration with silicon nitride photonic integrated circuit (PIC) platforms. He is a Co-Founder and Design Engineer with Solinide Photonics, where his work spans silicon nitride PIC fabrication and the development of the process design kit (PDK) for the company's multi-project wafer (MPW) platform.

Åsa Haglund (Member, IEEE) received the M.Sc. degree in physics from Gothenburg University, Sweden, and the Ph.D. degree in electrical engineering from the Chalmers University of Technology, Gothenburg, Sweden, in 2005. Since 2018, she has been a Professor with the Chalmers University of Technology and Visiting Researcher with Ulm University, Ulm, Germany, and Lund University, Sweden. Her research interests include III-nitride lasers and light-emitting diodes foremost in the visible and ultraviolet wavelength regions. The focus is on nanostructuring for new optical functionality and thin-film devices realized by electrochemical etching which enables vertical-cavity surface-emitting lasers (VCSELs) and photonic crystal surface-emitting lasers (PCSELs). Research achievements are proposed schemes to combat a large optical loss mechanism in blue VCSELs, which has contributed to today's state-of-the-art devices, the realization of the world's shortest emission wavelength from a VCSEL at the time at 300 nm, methodologies for accurate cavity length control in deep-UV VCSELs and the shortest emission wavelength from an ultraviolet PCSEL. She was the Program Chair for the International Conference on Nitride Semiconductors in Malmö, Sweden, 2025 and is on the advisory board for the same conference, the International Workshop of Nitride semiconductors, and International Workshop on Ultra-wide bandgap Materials and Devices and in the program committee for IWN, ICNS, SPIE Photonics West, and the GaN Marathon. She was the recipient of a prestigious consolidator grant from the European Research Council (2020), has received the Hasselblad award (2012), supervisor of the year award at Chalmers (2021) and is on The Photonics 100 list for 2026 – a recognition for pushing the photonics industry forward.

Anders Larsson (Life Fellow, IEEE) received the M.Sc. and Ph.D. degrees in electrical engineering from the Chalmers University of Technology, Göteborg, Sweden, in 1982 and 1987, respectively. In 1991, he joined the faculty at Chalmers where he was promoted to Professor in 1994. From 1984 to 1985, he was with the Department of Applied Physics, California Institute of Technology, Pasadena, CA, USA. From 1988 to 1991, he was with Jet Propulsion Laboratory, Pasadena. He has been a Guest Professor with Ulm University, Ulm, Germany, Optical Science Center, University of Arizona at Tucson, Tucson, AZ, USA, Osaka University, Osaka, Japan, and the Institute of Semiconductors, Chinese Academy of Sciences, Beijing, China. He has authored or coauthored more than 600 scientific journal and conference papers and two book chapters. His research interests include vertical-cavity surface-emitting lasers and optical interconnects. He co-organized the IEEE Semiconductor Laser Workshop 2004, organized the European Semiconductor Laser Workshop 2004, was a co-program Chair of European Conference on Optical Communication 2004, and Program and General Chair of IEEE International Semiconductor Laser Conference in 2006 and 2008, respectively. He was a Member of the IEEE Photonics Society Board of Governors during 2014–2016, Associate Editor for IEEE/OSA JOURNAL OF LIGHTWAVE TECHNOLOGY during 2011–2016, and Member of the Editorial Board of IET Optoelectronics during 2007–2020. In 2016, he co-founded OptiGOT AB, which was acquired by Nvidia in 2020, where he worked till 2025. His scientific background is in the areas of optoelectronic materials and devices for optical communication, information processing, and sensing. He is a Fellow of OSA and EOS. In 2012, he was the recipient of the HP Labs Research Innovation Award.